Feasibility of Cislunar Spacecraft Wake Generation

Kaylee Champion* and Hanspeter Schaub[†]

Department of Aerospace Engineering Sciences, University of Colorado Boulder, CO, 80303

Novel active and passive touchless potential sensing of neighboring spacecraft has been investigated for application in the Geosynchronous region. As interest in the cislunar region increases, this technology may be extended there as well. However, the cislunar plasma environment presents challenges not previously encountered in GEO, including spacecraft wake formation. To analyze how spacecraft wakes impact touchless potential sensing, cislunar spacecraft wakes are first characterized using NASCAP-2k and SIMION. The results are then used as the basis for the setup of experimental tests. To simulate cislunar wakes in the ECLIPS vacuum chamber at the University of Colorado Boulder, lens designs are investigated to expand and refocus the ion beam, referred to as telescoping. Optimization algorithms are used to determine the lens design, and the challenges and results are presented.

I. Introduction

Novel active and passive potential sensing has been investigated for application in the Geosynchronous region (GEO) [1–4]. Active potential sensing involves a servicing spacecraft directing an electron beam at a target so that secondary electrons [5, 6] and x-rays [7, 8] are emitted from the surface, as shown in Figure 1. The use of a low-wavelength ultraviolet laser has also been investigated as a method to excite photoemissions from a target [9, 10]. Secondary electrons and photoelectrons are emitted with low energies, so when they reach the servicer they have been accelerated approximately to the beam energy minus the potential difference between the servicer and target. The incoming signals are then measured, and the servicer utilizes the measurements to infer the potential of the target with respect to its own potential. Passive potential sensing works in a similar manner, but instead of exciting emissions with an electron beam, natural emissions, including secondary electron and photoelectron emissions, caused by the ambient space and plasma environment are measured. Knowledge of a target's potential can be used to account for electrostatic perturbations during docking [11, 12] and minimize the risk of discharges during close proximity operations [13]. Awareness of a target's potential is also the first step towards electrostatic actuation, which can be used to detumble or reorbit uncooperative targets, dock incoming bodies, and conduct touchless in-situ servicing [8, 14, 15].

An increasing number of missions have been sent and are scheduled for launch to the cislunar region, such as NASA's twin Acceleration Reconnection Turbulence and Electrodynamics of Moon's Interaction with the Sun (ARTEMIS) spacecraft, China's Chang'E-1 spacecraft, and the Lunar gateway [16–18]. Therefore, there is interest to extend touchless potential sensing technology to the cislunar region as well. However, the cislunar environment presents novel challenges not previously encountered in GEO. These including widely varying plasma parameters, short Debye lengths [19], and spacecraft wakes. This study focuses on enabling the investigation of cislunar spacecraft wakes impact on touchless potential sensing. When a spacecraft travels through plasma, the impacting electrons and ions are disturbed and pushed out of the way, similar to how an airplane or boat pushes air and water aside, respectively, as it travels. Then, a spacecraft wake may form when the spacecraft is mesothermal with respect to the plasma. This means that the thermal velocity of the electrons is greater than the velocity of the spacecraft with respect to the plasma and the thermal velocity of the ion is less than the spacecraft velocity ($v_i < v_{sc} < v_e$). So, the ions are not able to catch back up to the spacecraft, leaving a complex ion void region in the anti-velocity side of the spacecraft with respect to the plasma. The electrons are able to catch back up to the spacecraft, but the absence of ions on the wake side of the spacecraft creates a net negative charge region. This then repels electrons, limiting the number of electrons in the wake as well [20]. The plasma in GEO in not mesothermal, so the impact of wakes on touchless potential sensing has not been investigated.

The goal of this study is to characterize cislunar wakes and design an experimental setup such that researchers may follow a similar process to create wake experiments and cislunar wakes may be simulated in the ECLIPS vacuum chamber at the University of Colorado [21]. An overview of the cislunar plasma environment is presented in Section II, characterization of cislunar spacecraft wake formations is presented in Section III, previous work conducted to enable

---

*Graduate Research Assistant, Department of Aerospace Engineering Sciences, University of Colorado Boulder.

[†]Professor, Schaden Leadership Chair, Department of Aerospace Engineering Sciences, University of Colorado Boulder.
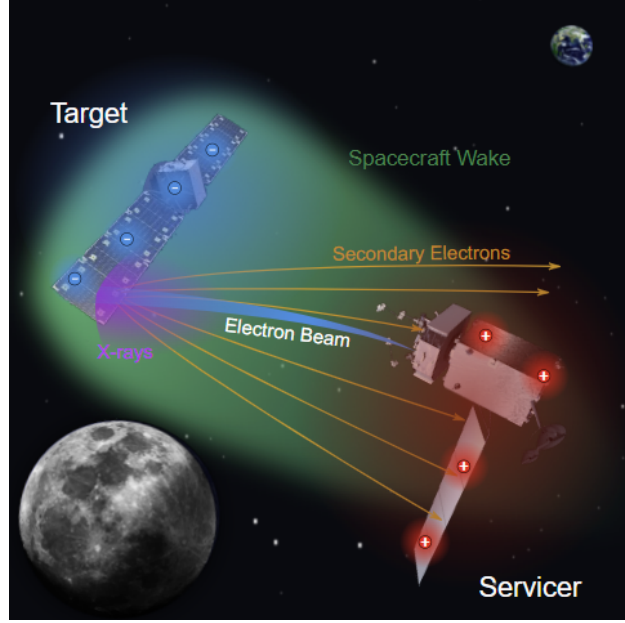
Fig. 1   Touchless potential sensing in cislunar space concept

representative LEO wakes in the ECLIPS chamber is presented in Section IV, and the cislunar wakes wakes design process in the ECLIPS chamber is presented in Section V.
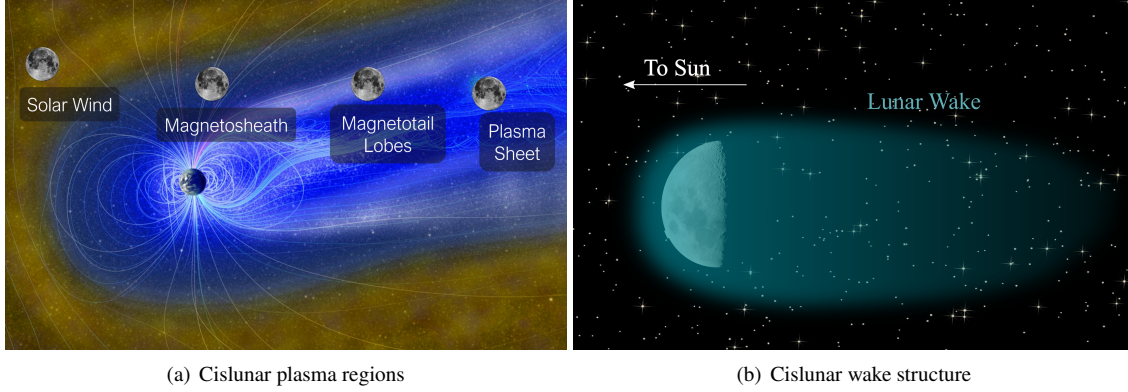
II. Cislunar Plasma Environment

The cislunar plasma environment can be divided into four regions: solar wind, magnetosheath, magnetotail lobes, and plasma sheet, as shown on the left side of Fig. 2 [22, 23]. The solar wind region is located outside Earth's magnetic field in the interplanetary magnetic field (IMF) and flowing solar wind. The magnetotail lobes are located inside the magnetopause and mainly consist of plasma outflow from the ionosphere. The plasma sheet is a region of hot plasma located in the center of the magnetotail that magnetically maps to the auroral oval and splits the magnetotail into its top and bottom lobes. It consists of plasma from the solar wind and ionosphere. The magnetosheath is located between the bow shock and magnetopause and is the transition region between the magnetotail lobes and the solar wind. It mainly consists of solar wind plasma that is deflected around the magnetopause [24]. Average characteristic parameters of these regions are shown in Table 1 [22].

Table 1   Cislunar regions average characteristic parameters [22]

Region	n_e $(1/m^3)$	T_e (eV)	v_i (km/s)	n_i $(1/m^3)$	T_i (eV)	λ_D (m)
Magnetotail Lobes	2.0E5	48	170	2.0E5	290	115.2
Plasmasheet	2.2E5	150	110	2.0E5	780	194.1
Magnetosheath Dayside	9.5E6	18	350	8.0E6	94	10.2
Solar Wind Dayside	6.0E6	11	420	6.0E6	7	10.1
Magnetosheath Wake (100km - 2000km)	1.9E5	50	260	1.9E5	330	120.58
Magnetosheath Wake (>12000km)	9E6	17	340	7.7E6	84	10.21
Solar Wind Wake (100km - 500km)	7.3E4	60	260	8.1E4	320	213.10
Solar Wind Wake (>12000km)	2.5E6	19	400	3E6	66	20.49

In addition to orbiting through several environments, when the moon is in the solar wind or magnetosheath region a

(a) Cislunar plasma regions

(b) Cislunar wake structure

Fig. 2   Cislunar environment variations

lunar wake will develop. The moon removes plasma from the environment through processes such as absorption and reflection. If no other processes occurred, this would leave a cylindrical vacuum in the anti-sunward side of the moon, as the flowing solar wind is approaching the moon from the sun. However, plasma re-enters through various processes, leaving a low density, complicated plasma structure on the nightside of the moon [25], as shown on the right side of Fig. 2. The properties of the wake varies with altitude, as the plasma returns to its undisturbed, ambient condition farther from the surface, as shown in Table 1. Therefore, the spacecraft wake formation and charge will also vary with altitude in the cislunar wake region.
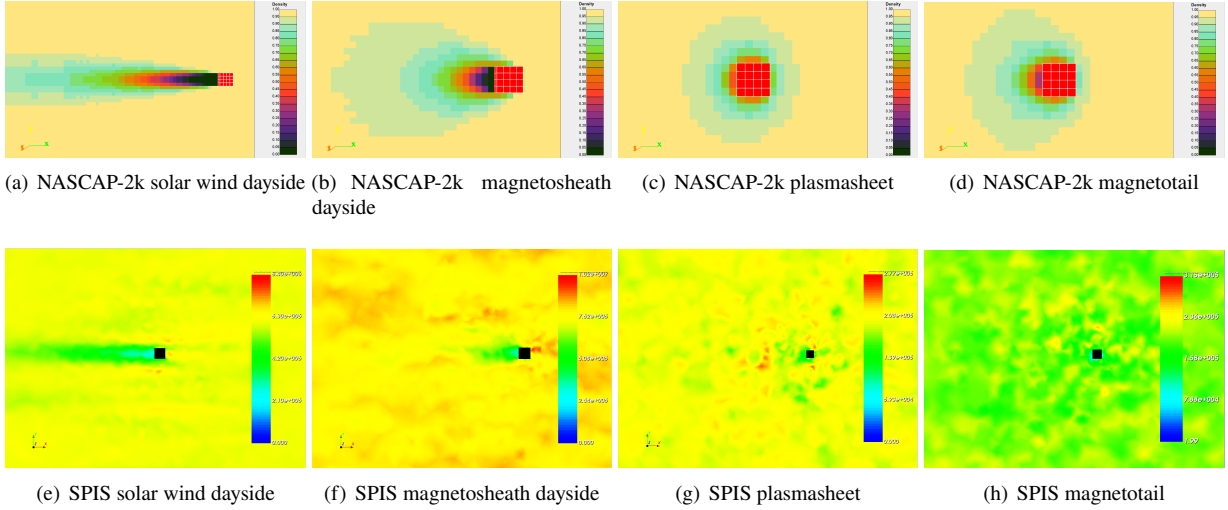
III. Wake Formation Investigation

In order to determine the cislunar regions in which spacecraft wakes may be expected and the shape and size of these wakes, the parameters in Table 1 were used to perform computations in NASCAP-2k and SPIS. NASCAP-2k is a 3D spacecraft charging and plasma interactions code developed as a collaboration between NASA and the Air Force Research Lab [26, 27]. SPIS is a spacecraft plasma interaction software created by the plasma interactions network in Europe (SPINE) [28, 29]. Both programs operate with the same basic principles: the object's geometry and computational space are defined, the plasma properties are specified, and methods of evaluation are selected. However, the methods in which the two programs determine the ambient plasma environment vary, and utilizing both tools allows the results to be verified. In order to ensure comparable results, a 1x1x1 m aluminum cube is used in both NASCAP-2k and SPIS, the cube is held to 0 Volts, and the ions are assumed to be 100% H^+. The magnetic field is neglected as the gyroradius in these regions is on the order of kilometers, larger than the computational volume [19].

The computational space is defined in NASCAP-2k using a Cartesian grid. The external boundary of the grid is defined as a 40x30x30 m rectangular prism with the spacecraft at a position of (25,15,15) meters in the grid. This allows for a distance of 15 meters from the external boundary, with extra computational space on the wake side of the spacecraft. The external boundary of the grid has a resolution of 1 meter, and the resolution of the grid around the spacecraft surface is 0.25 meters. To investigate the wakes in NASCAP-2k, the "Geometric Wake" option is utilized. This option computes the wake of the defined, uncharged spacecraft by determining the fraction of the Maxwellian plasma that is not blocked by the spacecraft at each grid point [27]. The results are then presented as a fraction of the ambient density.

In SPIS, the computational space is defined using a mesh. The external boundary is again defined as a 40x30x30 m rectangular prism with the spacecraft at a position of (25,15,15) meters in the grid. The resolution is also set equal to NASCAP-2k, with a resolution of 1 m at the external boundary and 0.25 m at the surface of the spacecraft. The mesh is then refined in Gmsh, a 3D finite element mesh generator and has a total of 158,663 tetrahedra after refinement. Once the computational space is defined, the Poisson equation is solved in order to determine the ambient plasma properties. In order to accurately model the ion and electron reactions to a moving spacecraft, the ions are modeled using a full particle-in-cell (PIC) simulation, and the electrons are modeled using a Maxwell-Boltzmann distribution. The ion charge density is then used to observe the spacecraft wake formation.

It is important to note that the spacecraft wake forms on the eclipse side of the spacecraft, as the bulk velocity, v_i in Table 1, of the plasma significantly exceeds the velocity of the spacecraft. In other words, the wake still forms on the anti-velocity side of the spacecraft, but the anti-velocity side of the spacecraft is always the eclipse side due to the high

(a) NASCAP-2k solar wind dayside (b) NASCAP-2k magnetosheath dayside (c) NASCAP-2k plasmasheet (d) NASCAP-2k magnetotail

(e) SPIS solar wind dayside (f) SPIS magnetosheath dayside (g) SPIS plasmasheet (h) SPIS magnetotail

Fig. 3 Cislunar spacecraft wake simulation results in NASCAP-2k and SPIS. The NASCAP-2k neutral wake results are shown on the top row, and the SPIS ion charge density results are shown on the bottom row.

speed of the solar wind. The differs from spacecraft wakes typically encountered in low earth orbit (LEO), as LEO plasma rotates with Earth. Thus, the wake side of the spacecraft coincides with the anti-velocity side with respect to an inertial frame [20].
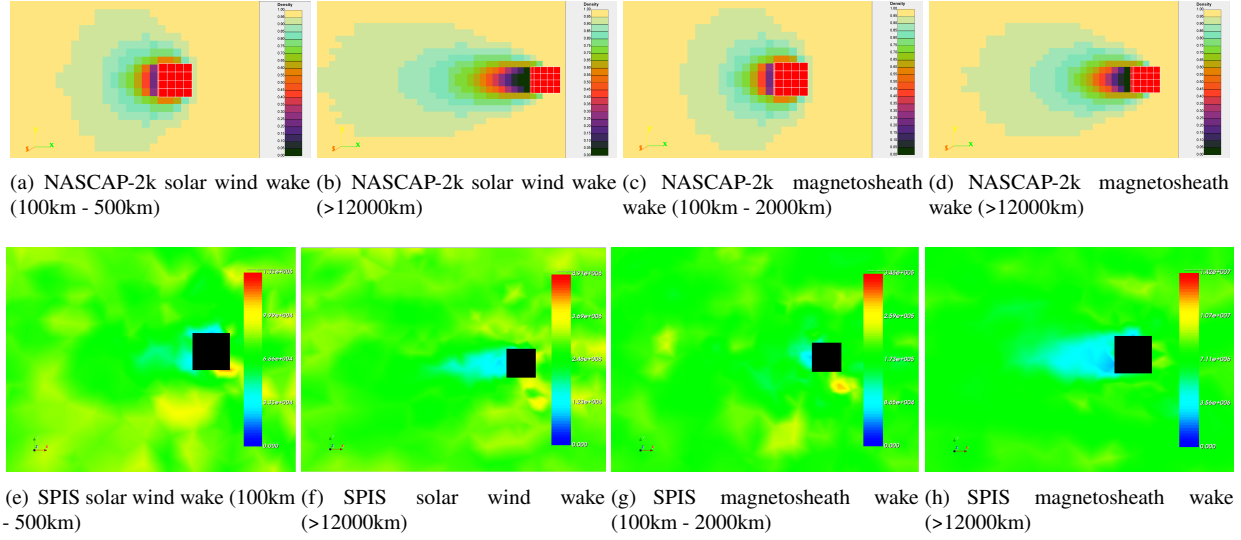
The wake simulation results for the parameters listed in Table 1 are shown in Fig. 3. In the solar wind dayside region, there is a clear wake that extends several times the length of the spacecraft. In addition, the wake has a large ion void region that extends a two or three spacecraft lengths. This intense wake formation in the solar wind matches previous solar wind wake investigation in SPIS conducted in references [30] and [31], which further validates the wake simulations. A wake also forms in the magnetosheath dayside regions in both computational tools. The magnetosheath wake is smaller than the solar wind wake, and the deepest part of the wake is less than one spacecraft width. This likely occurs because the ion temperature is higher, and the bulk speed of the ions is lower, allowing ions to catch up to the spacecraft more quickly. This weaker wake likely still create unexpected issues or benefits for touchless potential sensing technology and is of interest to investigate. In the plasmasheet and magnetotail regions, a spacecraft wake does not form, as shown. This makes sense, as the ion temperature is significantly higher and the bulk velocity is lower in these two regions. Thus, the ions and electrons are able to quickly catch back up to the spacecraft.

The plasma parameters also change with respect to altitude when the spacecraft is in the cislunar wake. The parameters listed in Table 1 are again used to investigate how the wake changes as the spacecraft altitude changes in the cislunar wake, and the results are shown in Fig. 4. As shown, closer to the surface of the moon, the ion temperature, or energy, is higher and the wake does not have a completely ion void region and extends less than one spacecraft length. In fact, this more rarefied, or less intense and smaller, wake can likely be neglected. In addition, close to the surface in the cislunar wake the plasma properties in the solar wind and magnetosheath region are similar, resulting in nearly identical NASCAP-2k and SPIS results. As the altitude of the spacecraft increases, the ion temperature decreases and the bulk velocity increases, leading to a wake formation. At greater than 12,000 km in altitude, there is a clear wake formation in both regions, but cislunar wake is still altering the plasma potentials. As a result, the wake is still smaller than those in the dayside regions. As shown, the spacecraft wake formation is more unpredictable in the cislunar wake, and use or avoidance of the wake during touchless potential sensing must be conducted with care.

IV. Previous Work

The chamber's ion gun, a Nonsequitur Technologies 1402 Ion Gun produces Ar^+ ions at an initial radius of approximately 1mm. Previous characterization of the chamber found that the beam spreads due to an initial expansion angle and space-charge effects, or the ions repelling each other, and may expand a diameter of approximately 1 cm [21]. In order to conduct wake experiments, an object, or primitive, may be placed in the ion beam, creating a wake region on the anti-velocity side of the primitive. However, a 1 cm diameter beam is not sufficient to conduct wake

(a) NASCAP-2k solar wind wake (100km - 500km)
(b) NASCAP-2k solar wind wake (>12000km)
(c) NASCAP-2k magnetosheath wake (100km - 2000km)
(d) NASCAP-2k magnetosheath wake (>12000km)

(e) SPIS solar wind wake (100km - 500km)
(f) SPIS solar wind wake (>12000km)
(g) SPIS magnetosheath wake (100km - 2000km)
(h) SPIS magnetosheath wake (>12000km)

Fig. 4   Cislunar spacecraft wake simulation results in the cislunar wake region in NASCAP-2k and SPIS. The NASCAP-2k neutral wake results are shown on the top row, and the SPIS ion charge density results are shown on the bottom row.

studies. Therefore, it has been proposed to implement ion optics to expand and then refocus the ion beam, referred to as telescoping, as shown in Fig. 5. A feasibility analysis of LEO wake generation in the chamber was conducted by a previous member of the Autonomous Vehicles Systems (AVS) lab [32]. To do so, SIMION, a particle tracing software package used to calculate electric fields and trajectories of charged particles, was utilized. SIMION computes the trajectory of each charged particle from Newton's second law

$$\frac{\mathrm{d}\mathbf{v}}{\mathrm{d}t} = \frac{q}{m}\mathbf{E},$$ (1)

where $\mathbf{v}$, q, and m are respectively the particle velocity, charge, and mass, $\mathbf{E}$ is the electric field, and t is the time. The electric field is derived from the electrostatic potential field V as

$$\mathbf{E} = \nabla V,$$ (2)

while V is computed by solving Laplace's equation

$$\nabla^2 V = 0$$ (3)

in the simulation domain. SIMION employs a regular Cartesian mesh with boundary conditions determined by set potentials of each electrode (Dirichlet) or by the zero-derivative of the V (Neumann). It is important to note that SIMION, by default, does not solve Poisson's equation to account for space-charge effects. So, spreading of the ion beam due to space charge effects is not accounted for. Instead, the beam is given an initial divergence angle of 1°.

The wake experiment is limited by experimental volume available in the ECLIPS chamber, which has a height of approximately 1 m and a diameter of approximately 75 cm [21]. In order to leave sufficient room for experiments to be conducted, the ion optics length and width are limited to 50 cm. Furthermore, previous work with the LEO wake simulation focused on wake shaping, so it was desirable for the potential of the plasma to approach zero before the edge of the ion beam in order to avoid edge effects and the primitive impacting the particle trajectories. To enable this, the Debye length of the plasma should be shorter than the distance from the primitive edge to the edge of the beam. The ion Debye length is

$$\lambda_D = \sqrt{\frac{\epsilon_0 k_B T_i}{n_i q_e^2}},$$ (4)

where ϵ_0 is the permittivity of free space, k_B is Boltzmann's constant from eV to Joules, T_i is the ion temperature in eV, n_i is the ion density in 1/m³, and q_e is the elementary charge in Coulombs. The density of the ions in the ECLIPS
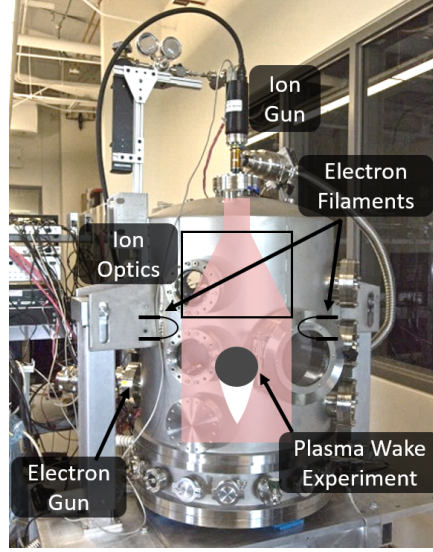
Fig. 5   ECLIPS proposed plasma wake implementation

chamber is [32]

$$n_i = \frac{I_{\text{beam}}}{q_e A v} = \frac{I_{\text{beam}}}{q_e \pi r^2} \sqrt{\frac{m_i}{2E}}, \tag{5}$$

where A is the final area of the beam, or πr^2, v is the velocity of the ions, and E is the energy of the ions, found as $E = 1/2 m_i v^2$ where m_i is the mass of the ions. Therefore, a wider beam results in a lower density and longer Debye length. In other words, a wide beam allows for a larger object to fit, but the potential will drop off slower and may not reach zero before the edge of the beam. If it is not feasible for the potential to reach zero before the edge of the beam, at minimum the primitive should be completely enveloped in the beam.

Despite the limited size of the ECLIPS chamber, large scale phenomenon may still be represented. A scaling law can be applied to relate the spacecraft's experimental radius R_0 to the radius in the environment of interest R_{sim} [33]

$$R_{\text{sim}} = \sqrt{\frac{n_i}{n_{sim}}} R_0 \tag{6}$$

Where n_i is the experiment plasma density and n_{sim} is the environment plasma density. In other words, if the density of the experimental ion beam is larger than the environmental plasma density, the experimental object represents a larger spacecraft. This relationship was derived for LEO plasma-body interactions, but it applies to processes governed by the Vlasov-Maxwell equations [33]. In addition, the Ar$^+$ ions generated in the ECLIPS chamber are not representative of most plasma environments. Fortunately, there is another scaling law that may be used to relate the velocity of two different ion species

$$v_{\text{sim}} = \sqrt{\frac{m_i}{m_{\text{sim}}}} v, \tag{7}$$

where v_{sim} is the velocity of the environment being simulated and m_{sim} is the mass of the ions in the simulated environment.

Two lens designs were investigated to telescope the ion beam: two thin lenses and three thick lens, as shown in Fig. 6. The thin lenses are designed as flat, thin plates with openings of radius R_{lens} to allow the beam to pass through. The thick lenses are thin cylindrical shells that again allow the ion beam to pass through the center. The lenses potentials V_{lens} and positions are then adjusted such that the ion beam is widened as wide as possible and refocused. Lens designs were then investigated by manually altering the lens parameters in SIMION, and the optimal design for LEO wakes was found using the thick lens telescope design, parameters and final radius are shown in Table 2. The final radius r_f is 3.5 cm, which is sufficient for placing a primitive in the wake. However, the velocity of the ions simulate those in LEO, not cislunar space, and the wake intensity and shape will differ from the cislunar spacecraft wakes of interest. Therefore, this design may still be used as a feasibility study of sensing through a wake, but it is desirable to better simulate cislunar wakes.

(a) Thin lens design   (b) Thick lens design
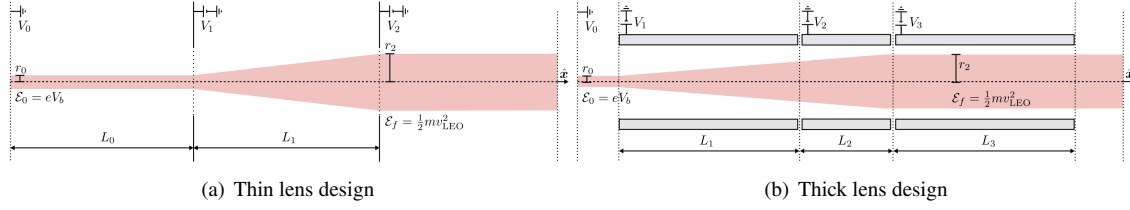
Fig. 6   Thick and thin lens telescoping design

Table 2   Optimal LEO telescope design parameters

E (eV)	V_1 (V)	V_2 (V)	V_3 (V)	L_1 (cm)	L_2 (cm)	L_3 (cm)	r_0 (cm)	r_f (cm)
40	-210	39	40	14	5	14	0.1	3.5

V. Chamber Wake Design

As mentioned previously, the LEO wake design for the ECLIPS chamber may be used to generate a wake in the chamber. A representative LEO wake could be used to test the feasibility of sensing through a wake, but different wake parameters may have different impacts on potential sensing. Therefore, it is desirable to generate representative cislunar wakes in the ECLIPS chamber. As shown in Section III, the most intense wake formation is seen in the solar wind dayside region. In addition, the moon spends approximately two thirds of its orbit in the solar wind [34], so generating representative dayside solar wind wakes is the focus of this study. The properties of the wake will be measured by a spherical Langmuir probe and 1.2 cm diameter RPA. So, a primitive larger than 1.2 cm in diameter, or larger than a 6 mm radius, must be able to fit inside the ion beam, and there should be a distance of at least 1.2 cm between the edge of the beam and the primitive, as this will enable to RPA to take measurements in and out of the wake. Thus, the minimum final beam diameter is 3.6 cm, or a radius of 18 mm.

A. Optimization Setup

First, the energy of the ion beam is chosen such that the velocity of the Ar^+ ions is representative of the velocity of the H^+ ions in the solar wind. A speed of 400 km/s is used to represent the H^+ ions, and, using Equation 7, the representative speed of Ar^+ ions is 63.6 km/s, or a beam energy E_B of 835 eV. Once the desired beam energy is determined, three lens designs are considered: two thin lenses, three thin lenses, and three thick lenses. Full scale models of the lens designs and ECLIPS chamber are generated in SIMION with a resolution of 1 mm, and the ion beam is defined as a circular distribution with an initial radius of 1 mm and half angle of 1°, based on previous characterization of the beam [21].

Each lens has three configurable parameters: location (or thickness for the thick lens design), potential, and inner radius. The final design then has six to nine variables that may be investigated to generate a telescoping lens design. In order to efficiently optimize the design of the lenses, a windows batch file is written to enable MATLAB to alter lens parameters and run a simulation. Then, a genetic algorithm and fminsearch in MATLAB are used to minimize an associated costs function. A genetic algorithm is a method for solving constrained or unconstrained optimization problems based on a natural selection process that mimics biological evolution. The algorithm is proficient at finding the approximate absolute minimum for the entire problem space, but the solution is not as accurate as MATLAB's fminsearch. MATLAB's fminsearch is a nonlinear programming solver that finds the minimum of a specified function and is proficient at determining local minimum near a defined starting point. Therefore, a genetic algorithm is first implemented, as the results are used as the initial guess for the fminsearch, optimizing the capabilities of both functions.

The goal of this study is to maximize the final radius of the beam and minimize the spread of the beam in the direction parallel with the ground of the chamber, which is defined as the y-direction in SIMION. In addition, the lenses may accelerate the ions, so the difference between the final velocity and 63.6 km/s should be minimized. The cost function is then

$$\text{Cost} = w_y \frac{n}{y_{\max}^2} + w_{v_y} \text{sum}(v_y^2) + w_{v_x} \text{sum}((v_x - 63.6)^2), \qquad (8)$$

where $y_{\max}$ is the maximum radius achieved by an ion particle, n is the number of particles, w_y is the weight appled the final radius, v_y is the final velocity in the y-direction, w_{v_y} is the weight applicable to minimizing the spread of the particles in the y-direction, v_x is the velocity in the x-direction, and w_{v_x} is the weight applicable to minimizing the

Table 3   Lens design constraints

Parameter	Constraints
E_B	$825 < E_B < 845$ eV
V_{lens}	$-30E3 < V_{lens} < 30E3$ V; $\quad V_1 < 0$ V
R_{lens}	$10 < R_{lens} < 250$ mm
x_{lens}	$x_3 > x_2 + 1cm > x_1 + 1cm$; $\quad x_1 > 100$ mm; $\quad x_2 < 500$ mm (2 thin lenses); $\quad x_3 < 500$ mm (3 thin lenses)
L_{lens}	$L_1 + L_2 + L_3 < 380$ mm

variance of the final velocity from the defined optimal velocity. The maximum radius is multiplied by the number of particles to make the values of each part of the cost function comparable, as the velocity components sum of the velocity of each particle. In addition, only the maximum value of the end position is used because particles that impact near the center of the chamber result in an uncharacteristically high cost function, skewing the results. Last, if potential of the lens is too high, the particles will be attracted back towards the lens and impact it. To avoid this, if the final position of the particles are not at the floor of the chamber, the cost function is given a value of 1E10 so that the design is not considered.

The constraints must be selected such that the final lens design fits inside the available experimental area and is within the bounds of the technology available in the ECLIPS chamber. The beam energy E_B is allowed to vary ±10 eV from the optimal energy in order to account for change in velocity due to the lenses, and the possible potential of the lenses V_{lens} is constrained by the capabilities of the Matsusada AU-30R1 High-Voltage Power Supplies (HVPS), or ±30E3 V. The radius of the space in the center of the lenses R_{lens} is set to a minimum of 10 mm and a maximum of 250 mm in order to allow space for stands to be installed on the outside of the lenses. Next, the location of the thin lenses x_{lens} must be greater than the exit of the ion gun, which extends 10 cm into the chamber, and less than 50 cm so that there is space to conduct the wake experiment. Last, the thick lenses must fit between the ion gun exit and 50 cm with 1 cm of space between the lenses. In other words, the combined length of the lenses L_{lens} must be less than 380 mm. These constraints are shown in Table 3.

B. Potential Field Sensitivity

The original SIMION model of the ECLIPS chamber included a simple model of the grounded chamber walls, the lenses, and the source of the Ar^+ particles located 10 cm from the top of the chamber, where the exit of the ion gun is located. When optimizing this setup, the ion often behaved in unexpected, troubling manners. For example, the ions would gain enough energy to leave the exit of the lenses, but not enough to impact the floor of the chamber. As a result, the ions oscillate between the lenses and never impact the lenses or chamber walls. The SIMION run is complete when all the particles have impact an object and stopped moving, so this oscillation leads to infinitely long simulations. In addition, the ions would often be attracted back towards and impact low potential lenses compared to the beam energy. Upon investigating the potential energy contours in SIMION, it was found that the curved top of the chamber resulted in a non-zero potential energy at the source location of the ions, as shown on the left in Fig. 7. This caused the ions to fly at a lower energy than expected and fail to impact the chamber floor. This issue was not previously encountered, as the LEO lens designed was modeled with a flat, grounded plate instead of the curved top of the chamber at the source location of the ions. The issue was then solved by simply modeling the grounded ion gun, as this forced the potential field to be zero at the source of the ions and more accurately represents the experiment setup, as shown in the right of Fig. 7. This demonstrates the sensitivity of particle trajectories to variations in the potential field. Furthermore, the ion trajectories in SIMION should not be treated as exact, and the final lens design will likely need to be modified when set up in the ECLIPS chamber.
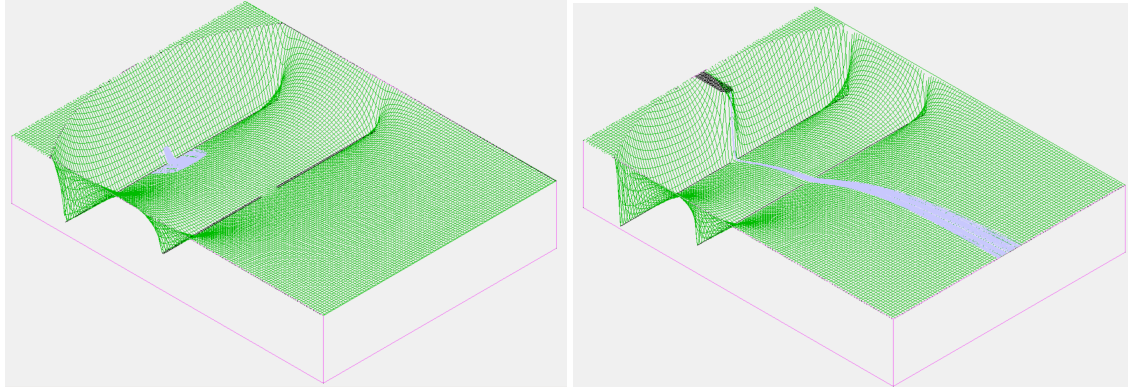
(a) SIMION potential energy view with no ion gun

(b) SIMION potential energy view with ion gun

Fig. 7   Potential energy contours of a two lens telescoping configuration in the ECLIPS chamber in SIMION. The left image has no ion gun modeled, and the right image has the grounded ion gun modeled. Ar^+ trajectories are shown in light purple.

C. Results

Once the chamber is properly modeled, the lens designs may be optimized. It is found that even when the maximum radius component of the cost function is multiplied by the number of particles, the velocity values are significantly higher. As a result, the optimization algorithms prioritize minimizing the divergence of the beam and stray from the optimal velocity, resulting in narrow, straight beams. So, w_{v_y} and w_{v_x} are set to zero, and w_y is set to one in order to prioritize maximizing the beam radius. The final design can then be altered post optimization to refocus the beam.

The optimized parameters and radius for the thin lens designs are shown in Fig. 8. The two thin lens design appears to widen the beam as soon as possible, as the first lens at the exit of the ion gun and is set to a large, negative potential. The second lens is then at a less negative potential and continues to widen the beam, resulting in a final radius of 63 mm. The three thin lens design again appears the widen the beam as soon as possible, as the first lens is at the exit of the ion gun and is set to a large, negative potential. However, the second lens has a large radius and is placed as close to the first lens as possible. This essentially moves the lens out of the way, simulating a two lens design. The final lens then has a large inner radius, but the large potential still expands the beam, resulting in a final radius of 71 mm.
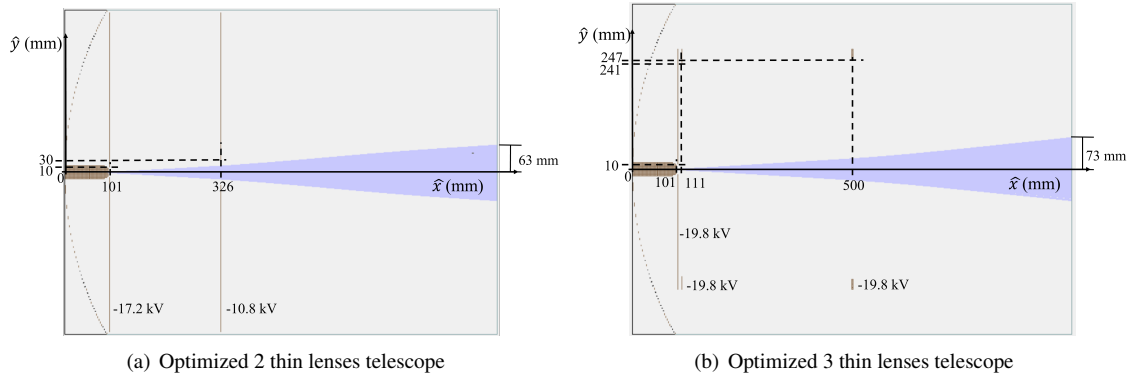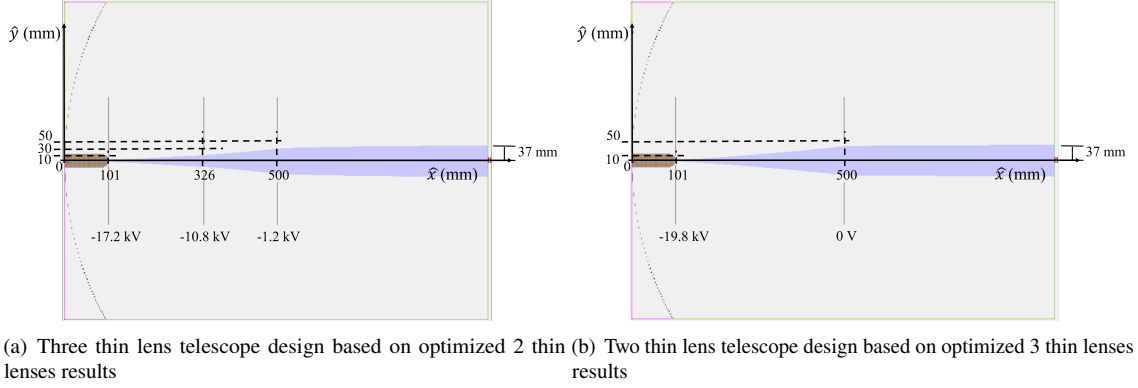

(a) Optimized 2 thin lenses telescope

(b) Optimized 3 thin lenses telescope

Fig. 8   Thin lens design results optimized to maximize the final radius of the ion beam. The energy of the ion beam is 831 eV for both designs.

These lens designs are sufficiently wide for the cislunar wake experiment, but the final beam is unfocused, creating a diverging flow that does not represent the flow of the solar wind. Therefore, a third "telescoping" lens is added to the original two thin lenses design, and the third lens in the original three lenses design is modified to refocus the beam. The resulting telescoped lens design is shown in Figure 9. Interestingly, both designs result in a final radius of 37 mm,
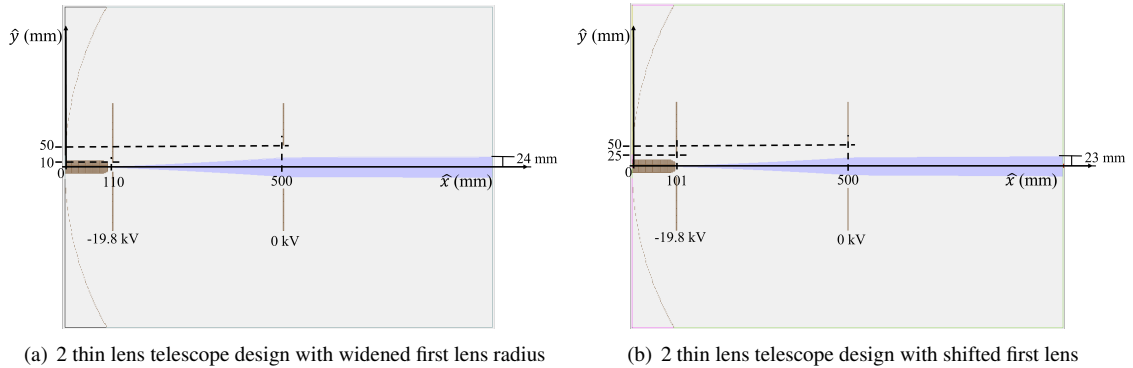
which mean that both original designs have a radius of 37 mm at the halfway point of the chamber. This allows for some flexibility in the final design, depending on if lower potentials or less lenses is a higher priority. In addition, the lens implemented to refocus the is not set to a positive potential for either design. This shows that to refocus the beam, the ions do not necessarily have to be repelled from the lens. Instead, there simply needs to be a sufficient potential difference between the lenses designed to expand the beam and those designed to focus the beam.

(a) Three thin lens telescope design based on optimized 2 thin lenses results

(b) Two thin lens telescope design based on optimized 3 thin lenses results

Fig. 9   Thin lens telescope designs based on designs optimized to maximize the final beam radius. The energy of the ion beam is 831 eV for both designs

The high potentials set on the first lens may cause arcs between the grounded ion gun and lens. To avoid this, the lens should have a separation distance of at least 1 cm from the ion gun. This is investigated in two ways for the two thin lens telescoping design: increasing the radius of the lens such that its 1 cm away and shifting the entire lens 1 cm away from the ion gun, as shown in Fig. 10. The final radii achieved is 23 mm when the lens is widened and 24 mm when the lens is shifted, decreasing the final radius by approximately 13 to 14 mm. The significant decrease in final radius demonstrates the importance of expanding the as soon as possible when designing a charged telescoping system. This is still sufficient for the experiments, as the radius exceeds the 168 mm minimum radius, allowing the RPA to take measurements in and out of the wake. In addition, for a beam current of 6 μA, the density n_i is approximately 3.264e11 $1/m^3$ from Equation 5, and a primitive with a 12 mm radius is representative of a 2.8 m radius spacecraft in 6E6 $1/m^3$ density plasma.

(a) 2 thin lens telescope design with widened first lens radius

(b) 2 thin lens telescope design with shifted first lens

Fig. 10   2 thin lens telescope design in which the first lens has a wider inner radius (left) and been shifted (right) so that the lens is separated from the ion gun by 1 cm in order to avoid arcing. The energy of the ion beam is 831 eV for both designs

The thick lens design is also considered. The lens design resulting from the optimization algorithms when maximizing the final radius is shown on the left on Fig. 11. This design initially expands the beam using two negative lenses, and then pushes the beam with a final, positive lens such that the particles rapidly expand in the opposite direction. Essentially, the potential energy of the particles is increased in the first two lenses and then released to expand

the particles, similar to pulling a bow and arrow back and then releasing it. This results in a wide final radius, but the particles are pushed through a point at the same time, which will likely cause unpredictable effects due to collisions. To avoid this design, the lenses are further constrained so that the particles cannot be repelled in the opposite direction. The maximum potential of the lenses is set to -3 kV, resulting in the design shown on the right side of Fig. 11. The final radius is 31 mm, but there is no refocusing of the beam, so the final beam design would have a smaller radius. Since a feasible beam expansion was achieved with a two thin lens design, and the final radius of the unfocused beam is approximately half that of the unfocused beam radii achieved by the thin lens designs, the thick lens design is not utilized.

(a) Optimized thick lens design

(b) Optimized thick lens design with lenses constrained to $V_{lens} <$ -3 kV
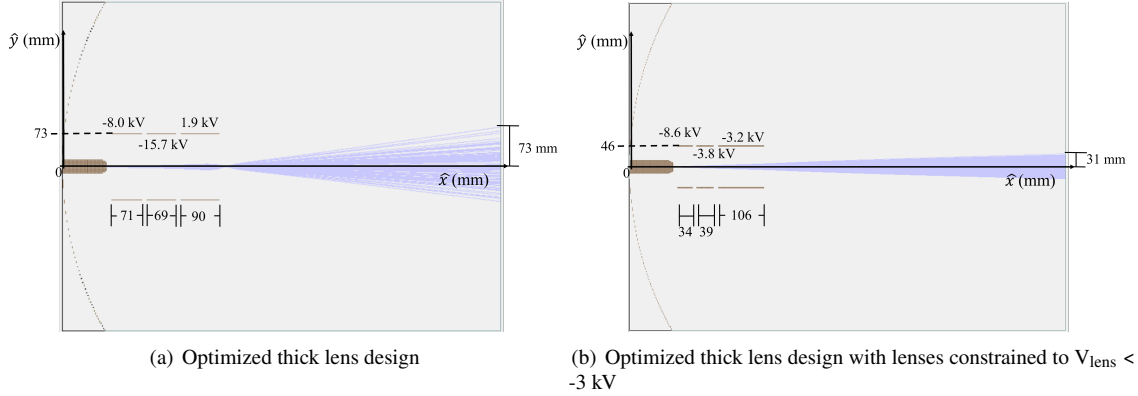
Fig. 11 2 thin lens telescope design in which the first lens has a wider inner radius (left) and been shifted (right) such that the lens is separated from the ion gun by 1 cm in order to avoid arcing. The energy of the ion beam is 831 eV for both designs

VI. Conclusion

Spacecraft wakes are shown to occur in the solar wind and magnetosheath regions. However, in the cislunar wake in these regions the spacecraft will not have a wake close to the lunar surface and may develop larger wakes as the altitude increases. This variations complicates consideration of wakes during touchless potential sensing, as there will be variations between environments and locations with respect to the moon. A lens design is then investigated to simulate solar wind wakes in the ECLIPS chamber, as this will allow experimental investigation of touchless potential sensing in the presence of a wake. An optimization scheme is introduced, and it is found that the optimal design is simply to expand the beam as soon as possible using a thin, high potential lens. The beam is then allowed to expand as long as possible and is refocused with a telescoping lens. This design results in a radius of 24 mm, which is sufficient for cislunar wake experiments.

Acknowledgments

References

[1] Bengtson, M., Wilson, K., Hughes, J., and Schaub, H., "Survey of the electrostatic tractor research for reorbiting passive GEO space objects," *Astrodynamics*, Vol. 2, No. 4, 2018, pp. 291–305.

[2] Hogan, E. A., and Schaub, H., "Impacts Of Tug And Debris Sizes On Electrostatic Tractor Charging Performance," *Advances in Space Research*, Vol. 55, No. 2, 2015, pp. 630–638. https://doi.org/10.1016/j.asr.2014.10.023.

[3] Hogan, E. A., and Schaub, H., "Impacts of Hot Space Plasma and Ion Beam Emission on Electrostatic Tractor Performance," *IEEE Transactions on Plasma Science*, Vol. 43, No. 9, 2014, pp. 3115–3129. https://doi.org/10.1109/TPS.2015.2451001.

[4] Hogan, E. A., and Schaub, H., "Space weather influence on relative motion control using the touchless electrostatic tractor," *The Journal of the Astronautical Sciences*, Vol. 63, No. 3, 2016, pp. 237–262. https://doi.org/10.1007/s40295-016-0090-4.

[5] Bengtson, M. T., Wilson, K. T., and Schaub, H., "Experimental Results of Electron Method for Remote Spacecraft Charge Sensing," *Space Weather*, Vol. 18, No. 3, 2020, pp. 1–12. https://doi.org/10.1029/2019SW002341.

[6] Romero-Calvo, Á., Hammerl, J., and Schaub, H., "Touchless potential sensing of complex differentially-charged shapes using secondary electrons," *AIAA SCITECH 2022 Forum*, 2022. https://doi.org/10.2514/6.2022-2311.

[7] Wilson, K. T. H., and Schaub, H., "X-Ray Spectroscopy for Electrostatic Potential and Material Determination of Space Objects," *IEEE Transactions on Plasma Science*, Vol. 47, No. 8, 2019, pp. 3858–3866. https://doi.org/10.1109/TPS.2019.2910576.

[8] Wilson, K. T., Bengtson, M. T., and Schaub, H., "X-ray Spectroscopic Determination of Electrostatic Potential and Material Composition for Spacecraft: Experimental Results," *Space Weather*, Vol. 18, No. 4, 2020, p. e2019SW002342. https://doi.org/10.1029/2019SW002342.

[9] Romero-Calvo, A., Champion, K., and Schaub, H., "Touchless Spacecraft Potential Sensing Using Energetic Electron Beams and Active Photoemissions," *16th Spacecraft Charging Technology Conference*, 2022.

[10] Romero Calvo, Á., Champion, K., and Schaub, H., "Enabling Ultraviolet Lasers for Touchless Spacecraft Potential Sensing," *IEEE Transactions on Plasma Science*, Vol. 0, No. 0, 2023, pp. 1–15. *in press*.

[11] Wilson, K., and Schaub, H., "Impact of Electrostatic Perturbations on Proximity Operations in High Earth Orbits," *Journal of Spacecraft and Rockets*, Vol. 58, No. 5, 2021, pp. 1293–1302. https://doi.org/10.2514/1.A35039.

[12] Wilson, K., Romero-Calvo, A., and Schaub, H., "Constrained Guidance for Spacecraft Proximity Operations Under Electrostatic Perturbations," *Journal of Spacecraft and Rockets*, Vol. 0, No. 0, 2022, pp. 1–13. https://doi.org/10.2514/1.A35162, *in press*.

[13] Schaub, H., Parker, G. G., and King, L. B., "Challenges and Prospects of Coulomb Spacecraft Formation Control," *The Journal of the Astronautical Sciences*, Vol. 52, No. 1, 2004, pp. 169–193. https://doi.org/10.1007/BF03546427.

[14] Casale, F., Schaub, H., and Biggs, J. D., "Lyapunov Optimal Touchless Electrostatic Detumbling of Geostationary Debris Using Surface Multisphere Models," *AIAA Journal of Spacecraft and Rockets*, Vol. 58, No. 3, 2021. https://doi.org/10.2514/1.A34787.

[15] Schaub, H., and Moorer, D. F., "Geosynchronous Large Debris Reorbiter: Challenges and Prospects," *The Journal of the Astronautical Sciences*, Vol. 59, No. 1, 2012, pp. 161–176. https://doi.org/10.1007/s40295-013-0011-8.

[16] Zhang, T., Sun, Y., and Tang, Z., "3D visualization of solar wind ion data from the Chang'E-1 exploration," *Computers & Geosciences*, Vol. 37, No. 10, 2011, pp. 1711–1718. https://doi.org/https://doi.org/10.1016/j.cageo.2011.01.016, URL https://www.sciencedirect.com/science/article/pii/S0098300411001130.

[17] Angelopoulos, V., "The ARTEMIS mission," *The ARTEMIS mission*, 2010, pp. 3–25. https://doi.org/https://doi.org/10.1007/978-1-4614-9554-3_2.

[18] Willis, E. M., Haviland, H. F., Minow, J. I., and Coffey, V. N., "A Comparison of ARTEMIS Data with the Lunar Plasma Design Environment for NASA Crewed Missions," *Applied Space Environments Conference 2019*, 2019.

[19] Champion, K., and Schaub, H., "Electrostatic Potential Shielding in Representative Cislunar Regions," *IEEE Transactions on Plasma Science*, Vol. 0, No. 0, 2023, pp. 1–13. *in press*.

[20] Lai, S. T., *Fundamentals of Spacecraft Charging: Spacecraft Interactions with Space Plasmas*, Princeton University Press, 2012.

[21] Wilson, K., Romero-Calvo, Á., Bengtson, M., Hammerl, J., Maxwell, J., and Schaub, H., "Development and characterization of the ECLIPS space environments simulation facility," *Acta Astronautica*, Vol. 194, 2022, pp. 48–58. https://doi.org/https://doi.org/10.1016/j.actaastro.2021.12.037.

[22] Leahy, F. B., "SLS-SPEC-159, Cross-Program Design Specification for Natural Environments (DSNE)," Tech. rep., National Aeronautics and Space Administration, 2021.

[23] Halekas, J., Saito, Y., Delory, G., and Farrell, W., "New views of the lunar plasma environment," *Planetary and Space Science*, Vol. 59, No. 14, 2011, pp. 1681–1694. https://doi.org/https://doi.org/10.1016/j.pss.2010.08.011.

[24] Pisacane, V. L., *The space environment and its effects on space systems*, American Institute of aeronautics and Astronautics, 2008.

[25] Zhang, H., Khurana, K. K., Kivelson, M. G., Angelopoulos, V., Wan, W. X., Liu, L. B., Zong, Q.-G., Pu, Z. Y., Shi, Q. Q., and Liu, W. L., "Three-dimensional lunar wake reconstructed from ARTEMIS data," *Journal of Geophysical Research: Space Physics*, Vol. 119, No. 7, 2014, pp. 5220–5243. https://doi.org/https://doi.org/10.1002/2014JA020111.

[26] Davis, V., Gardner, B., and Mandell, M., "Nascap-2k version 4.3 users manual," Tech. rep., LEIDOS HOLDINGS INC SAN DIEGO CA, 2016.

[27] Davis, V., and Mandell, M., "Nascap-2k Version 4.3 Scientific Documentation," Tech. rep., Leidos, Inc. San Diego United States, 2016.

[28] Sarrailh, P., Matéo-Vélez, J.-C., Hess, S. L. G., Roussel, J.-F., Thiébault, B., Forest, J., Jeanty-Ruard, B., Hilgers, A., Rodgers, D., Cipriani, F., and Payan, D., "SPIS 5: New Modeling Capabilities and Methods for Scientific Missions," *IEEE Transactions on Plasma Science*, Vol. 43, No. 9, 2015, pp. 2789–2798. https://doi.org/10.1109/TPS.2015.2445384.

[29] Hess, S., Sarrailh, P., Matéo-Vélez, J., Villemant, M., Leclerq, L., Jeanty-Ruard, B., and Trouche, A., "Spacecraft-Plasma Interaction Software V6," Tech. rep., SPINE, 2021.

[30] Eriksson, A. I., Khotyaintsev, Y., and Lindqvist, P.-A., "Spacecraft wakes in the solar wind," *Proceedings of the 10th Spacecraft Charging Technology Conference*, Vol. 6, 2007, pp. 18–21.

[31] Ergun, R. E., Malaspina, D. M., Bale, S. D., McFadden, J. P., Larson, D. E., Mozer, F. S., Meyer-Vernet, N., Maksimovic, M., Kellogg, P. J., and Wygant, J. R., "Spacecraft charging and ion wake formation in the near-Sun environment," *Physics of Plasmas*, Vol. 17, No. 7, 2010, p. 072903. https://doi.org/10.1063/1.3457484, URL https://doi.org/10.1063/1.3457484.

[32] Maxwell, J., "Development of Electrostatic Actuation Techniques for Close-Proximity Formation Flying in Low Earth Orbit Plasma Wakes," Ph.D. thesis, University of Colorado Boulder, Aug. 2020. URL https://hanspeterschaub.info/Papers/grads/JordanMaxwell.pdf.

[33] Capon, C. J., Brown, M., and Boyce, R. R., "Scaling of plasma-body interactions in low Earth orbit," *Physics of Plasmas*, Vol. 24, No. 4, 2017, p. 042901. https://doi.org/10.1063/1.4979191, URL https://doi.org/10.1063/1.4979191.

[34] Ness, N. F., "Interaction of the solar wind with the Moon," *Solar-Terrestrial Physics/1970*, Springer, 1972, pp. 347–393.